Green's function molecular dynamics
Including finite heights, shear, and body fields

Parayil Venugopalan, S.; Nicola, Lucia; Müser, Martin H.

DOI
10.1088/1361-651X/aa606b

Publication date
2017

Document Version
Final published version

Published in
Modelling and Simulation in Materials Science and Engineering

Modelling and Simulation in Materials Science and Engineering

PAPER • **OPEN ACCESS**

Green's function molecular dynamics: including finite heights, shear, and body fields

To cite this article: Syam P Venugopalan *et al* 2017 *Modelling Simul. Mater. Sci. Eng.* **25** 034001

OPEN ACCESS
IOP Publishing
Made open access 6 June 2017
Modelling and Simulation in Materials Science and Engineering
Modelling Simul. Mater. Sci. Eng. **25** (2017) 034001 (13pp) https://doi.org/10.1088/1361-651X/aa606b

Green's function molecular dynamics: including finite heights, shear, and body fields

Syam P Venugopalan[1], **Lucia Nicola**[1] **and Martin H Müser**[2]

[1] Department of Materials Science and Engineering, Delft University of Technology, 2628 CD Delft, The Netherlands
[2] Department of Materials Science and Engineering, Saarland University, 66123 Saarbrücken, Germany

Received 24 October 2016, revised 7 February 2017
Accepted for publication 14 February 2017
Published 2 March 2017

Abstract

The Green's function molecular dynamics (GFMD) method for the simulation of incompressible solids under normal loading is extended in several ways: shear is added to the GFMD continuum formulation and Poisson numbers as well as the heights of the deformed body can now be chosen at will. In addition, we give the full stress tensor inside the deformed body. We validate our generalizations by comparing our analytical and GFMD results to calculations based on the finite-element method (FEM) and full molecular dynamics simulations. For the investigated systems we observe a significant speed-up of GFMD compared to FEM. While calculation and proof of concept were conducted in two-dimensions only, the methodology can be extended to the three-dimensional case in a straightforward fashion.

Keywords: contact mechanics, tribology, Green's function

(Some figures may appear in colour only in the online journal)

1. Introduction

Green's function molecular dynamics (GFMD) [1–3] is a boundary-value method allowing one to simulate the linear-elastic response of a solid to an external stress or, more generally, to a boundary condition. So far, GFMD has been used predominantly to describe either non-reflecting [4, 5] and thermalizing [6–8] boundaries to which an atomistic region is coupled, or, as a tool to simulate the contact mechanics of solids with rough surfaces [9–11]. One advantage of GFMD is that it only necessitates knowledge of the displacements in the top layer of a solid and that effective interactions are block diagonal in Fourier space. Relatively large systems can therefore be simulated and be quickly relaxed. Typical system sizes in the

context of contact mechanics range from 4096×4096 surface atoms on single CPUs [9] to $O(10^5 \times 10^5)$ on supercomputers [11].

An additional, conceivable application consists in coupling GFMD to discrete dislocation dynamics (DDD) [12]. The idea is to use GFMD, instead of the finite-element method, to compute the image fields of dislocations in DDD. Towards this end, we generalize the GFMD method in the following ways: first, we consider the elastic response of a cubic or an isotropic body with arbitrary Poisson number and allow for lateral displacements as well as for shear tractions in addition to normal tractions. Second, we deduce the internal stresses for a given surface boundary condition and do this for solids of arbitrary height. The approaches pursued so far were limited to either normal displacements and normal tractions in the continuum formulation [11, 13] or to the full atomistic Green's functions [2, 9], which do not relate directly to the continuum limit. While the finite-width elastic continuum problem with shear was solved by Carbone and Mangialardi [14], their work did not put us into the position to deduce directly the Green's function coefficients needed for a numerical implementation. In a later work, in particular appendix A of [15], useful formulae for the GFMD simulations were stated, but unfortunately only for the frictionless case.

In this work, we present a solution for the Green's function of finite-height elastic slabs having the following advantages: the only required mathematical tools are partial derivatives, Fourier transforms, and linear algebra, i.e., there is no need to solve Fredholm integral equations. All equations needed to implement the approach into computer code are given explicitly in compact form. Moreover, our approach can be readily modified in various ways. For example, it should be straightforward to extend our solution strategy to layered materials, to materials with gradient or square-gradient corrections to the elastic energy, or to non-isotropic crystals—as long as they remain homogeneous within each plane. In fact, the most important equations for non-isotropic crystals are given and tested in this work. Lastly, we validate our solution against numerical data and moreover consider various limiting cases including that of very small slab heights or that of a vanishing shear modulus characteristic for fluids.

The coupling between GFMD and DDD will be presented in a separate manuscript.

2. Theoretical considerations

2.1. General background

In this paper, we are concerned with the quasi-static loading, in which case the precise dynamical response of the simulated layer does not play a role, see [5, 15, 16] for generalizations from the static to the dynamic case. Moreover, we consider to load the surface of a body that is translationally invariant within the *xy*-plane, which, in principle, is allowed to be a gradient material as long as the gradients are normal to the *xy* surface plane. One can then write the linear stress-displacement relation $u[\sigma(\mathbf{r})]$ as

$$u_\alpha(\mathbf{r}) = \int \mathrm{d}^2 r'\, G_{\alpha\beta}(\mathbf{r}')\, \sigma_{3\beta}(\mathbf{r} + \mathbf{r}'), \tag{1}$$

where $G_{\alpha\beta}(\mathbf{r}')$ is the Green's function tensor, $u_\alpha(\mathbf{r})$ is the α component of the displacement as a function of the (two-dimensional) in-plane coordinate $\mathbf{r}$, and $\sigma_{3\beta}$ is the traction in z-direction. In Fourier space, equation (1) reads

$$\tilde{u}_\alpha(\mathbf{q}) = \tilde{G}_{\alpha\beta}(\mathbf{q})\tilde{\sigma}_{3\beta}(\mathbf{q}). \tag{2}$$

In contact problems, one often knows the displacement of the bodies and wants to deduce the contact pressure, and thus, one usually does not need to evaluate the Green's function (tensor) itself, but its inverse. Thus, force calculations in GFMD simulations require one to evaluate

$$\tilde{\sigma}_{3\alpha}(\mathbf{q}) = [\tilde{G}^{-1}(\mathbf{q})]_{\alpha\beta}\tilde{u}_{\beta}(\mathbf{q}). \tag{3}$$

The precise functional form of the (inverse) Green's function tensor depends on the elastic properties of the deformed material including its height.

In its simplest form, usually used in the context of (continuum) contact mechanics [17], one is only interested in normal displacements induced by normal tractions applied to a semi-infinite, isotropic body. In this case, if the body is incompressible, $\nu = 0.5$, all quantities in equation (3) can be considered as scalars and the equation reduces to

$$\tilde{\sigma}(\mathbf{q}) = qE^*\tilde{u}(\mathbf{q})/2, \tag{4}$$

where $E^* = E/(1 - \nu^2)$ is the contact modulus, E being the Young's modulus and ν the Poisson number. However, as mentioned in the introduction, we wish to generalize GFMD to give the elastic response of a body with generic Poisson's ratio, and therefore, we can no longer use a scalar to describe surface displacement. Moreover, we intend to consider problems where contact loading is not restricted to be in normal direction, i.e. tractions and/or displacement can be applied in normal or tangential directions, everywhere on the body surface. Therefore, we can no longer rely on equation (4) and need to find a form for the Green's function tensor in equation (3), which has to depend on the Poisson's ratio and on the height of the slab. Towards this end, we next calculate the analytical solutions for the displacement in linearly elastic slabs of finite height, from which the stresses can be deduced in a straightforward fashion. The stress distribution underneath the contact are of particular interest in problems as fretting fatigue, to determine whether a possible tensile loading underneath the contact would give rise to crack nucleation and propagation.

2.2. Analytical solutions for the displacement in finite-height, linearly elastic slabs

We consider a linearly elastic body of cubic or higher symmetry in a slab geometry with a fixed bottom, i.e., the displacement reads $\mathbf{u}(x, z = 0) = 0$ rather than $\mathbf{u}(x, z \to -\infty) \to 0$ as for semi-infinite solids. Moreover, we assume that no body forces are exerted, which implies the usual equilibrium condition $\partial_\alpha \sigma_{\alpha\beta}(\mathbf{r}) = 0$, where $\sigma_{\alpha\beta}(\mathbf{r})$ is the stress at the point $\mathbf{r}$ inside the body and $\partial_\alpha \equiv \partial/\partial r_\alpha$. For isotropic or cubic bodies the equilibrium condition is given by

$$C_{11}\partial_1^2 u_1 + C_{44}\partial_3^2 u_1 + (C_{12} + C_{44})\partial_1\partial_3 u_3 = 0 \tag{5}$$

$$C_{11}\partial_3^2 u_3 + C_{44}\partial_1^2 u_3 + (C_{12} + C_{44})\partial_1\partial_3 u_1 = 0, \tag{6}$$

where we have restricted our attention to $(1 + 1)$-dimensional solids so that in-plane wavevectors are now scalars, and where the C_{ij}'s denote coefficients of the elastic tensor in Voigt notation.

Assuming an in-plane undulation of the top layer with the real-valued wavenumber q, equations (5) and (6) can be solved with the factorization

$$u_\alpha(x, z) = u_\alpha^0 \exp(\mathrm{i}qx)\exp(\mathrm{i}kz), \tag{7}$$

where k is a complex wavenumber satisfying

$$(k/q)^2 = -b \pm \sqrt{b^2 - 1} \tag{8}$$

with

$$b = \frac{C_{11}^2 + C_{44}^2 - (C_{12} + C_{44})^2}{2C_{11}C_{44}}. \tag{9}$$

Thus, we obtain solutions for the displacements either oscillating exponential functions for $b < 1$ or purely exponential functions for $b > 1$. The nature of the solution changes at $b = 1$, which automatically holds for isotropic media as these satisfy the isotropy condition $C_{44} = (C_{11} - C_{12})/2$. The solutions for $b = 1$ are proportional to $\exp(\pm qz)$, and, in addition, proportional to $z\exp(\pm qz)$, i.e., similar to those of critically damped harmonic oscillators. The decaying solutions can usually be ignored when the z-position of the top layer z_m satisfies $z_\mathrm{m} \gg 1/q$ but not for a finite-slab geometry.

In the remainder of this section, we focus on the isotropic case, because this is a common approximation. In the result section, we also consider the case of a cubic solid violating the isotropy condition to demonstrate the correctness of our approach. At this point, it may suffice to state that metallic cubic crystals tend to have a relatively small shear modulus, in which case $b > 1$, while non-metals rather correspond to $b < 1$.

Due to the nature of the differential equations (5) and (6), the solutions of the in-plane cosine transform of the lateral u_1 displacement field couples to the in-plane sine transform of the normal u_3 displacement, and vice versa. Thus, we can write

$$u_1^\mathrm{c}(x, z) = \cos(qx)\tilde{u}_1^\mathrm{c}(q, z) \tag{10}$$

$$u_3^\mathrm{s}(x, z) = \sin(qx)\tilde{u}_3^\mathrm{s}(q, z). \tag{11}$$

Solutions satisfying the boundary condition $\mathbf{u}(x, 0) = 0$ and the differential equation for isotropic media are then obtained after some algebra to satisfy

$$\begin{bmatrix} \tilde{u}_1^\mathrm{c}(q, z) \\ \tilde{u}_3^\mathrm{s}(q, z) \end{bmatrix} = \begin{bmatrix} f_1(qz) & -f_2(qz) \\ f_2(qz) & f_3(qz) \end{bmatrix} \begin{bmatrix} A_1 \\ A_2 \end{bmatrix} \tag{12}$$

with

$$f_1(qz) = \sinh(qz) + \frac{1 - s}{1 + s} qz\cosh(qz), \tag{13}$$

$$f_2(qz) = \frac{1 - s}{1 + s} qz\sinh(qz), \tag{14}$$

$$f_3(qz) = \sinh(qz) - \frac{1 - s}{1 + s} qz\cosh(qz), \tag{15}$$

where $s \equiv C_{44}/C_{11}$. The latter ratio has allowed values of $0 < s < 1$ for stable, two-dimensional isotropic solids [18]. The coefficients $A_{1,2}$ follow from equation (12) once $\tilde{u}_1^\mathrm{c}(q, z)$ and $\tilde{u}_3^\mathrm{s}(q, z)$ are given at $z = z_\mathrm{m}$, where z_m is the height of the undeformed solid. Lastly, the in-plane sine transform of u_1 and cosine transform of u_3 can be calculated in a similar fashion via:

$$\begin{bmatrix} \tilde{u}_1^\mathrm{s}(q, z) \\ \tilde{u}_3^\mathrm{c}(q, z) \end{bmatrix} = \begin{bmatrix} f_1(qz) & f_2(qz) \\ -f_2(qz) & f_3(qz) \end{bmatrix} \begin{bmatrix} B_1 \\ B_2 \end{bmatrix}. \tag{16}$$

In summary, for an arbitrary surface displacement field $\mathbf{u}(x, z_m)$, the in-plane Fourier transform is taken to yield $\tilde{\mathbf{u}}(q, z_m)$. The real and imaginary parts can be associated with left-hand sides of equations (12) and (16), which allow one to determine the pertinent coefficients $A_{1,2}$ and $B_{1,2}$ for each wavenumber q by evaluating them at $z = z_m$. The knowledge of these coefficients then allows one to deduce the displacement inside the body.

2.3. Finite-height-slab strain, stress, and energy density

Not only the displacement but also the strain and thus the stress field on the surface or inside the body can be deduced as soon as the coefficients $A_{1,2}$ and $B_{1,2}$ have been determined for a given surface topography, obtained by perturbation of an initially flat surface. For reasons of simplicity, we first restrict our attention to the case of a perturbation by a single wave number q and $B_{1,2} = 0$. The elements of the infinitesimal Cauchy's strain tensor (in Voigt notation) are then given by

$$\begin{aligned}\epsilon_1(x, z) &\equiv \partial_1 u_1(x, z)\\ &= -\, q \sin(qx)\tilde{u}_1^{\mathrm{c}}(q, z),\end{aligned} \tag{17}$$

$$\begin{aligned}\epsilon_3(x, z) &\equiv \partial_3 u_3(x, z)\\ &= \sin(qx)\partial_3\tilde{u}_3^{\mathrm{s}}(q, z),\end{aligned} \tag{18}$$

$$\begin{aligned}\epsilon_5(x, z) &\equiv \partial_1 u_3(x, z) + \partial_3 u_1(x, z)\\ &= \cos(qx)\{q\tilde{u}_3^{\mathrm{s}}(q, z) + \partial_3\tilde{u}_1^{\mathrm{c}}(q, z)\}.\end{aligned} \tag{19}$$

These expressions can now be used to compute the stresses inside the body as well as on its surface with the usual stress-strain relations. Knowledge of the latter suffices to determine the work per unit area needed to deform the body—assuming small surface slopes and thus the surface normal to be approximately parallel to the z-axis—via

$$v_{\mathrm{el}} = \frac{1}{L}\int_0^L \mathrm{d}x\left[\int_0^{u_1(x,z_m)} \sigma_{31}(x, z_m)\mathrm{d}u_1(x, z_m) + \int_0^{u_3(x,z_m)} \sigma_{33}(x, z_m)\mathrm{d}u_3(x, z_m)\right]. \tag{20}$$

This yields

$$v_{\mathrm{el}} = \frac{C_{44}}{2}\tilde{\epsilon}_5^{\mathrm{c}}(q, z_m)\tilde{u}_1^{\mathrm{c}}(q, z_m) + \left\{\frac{C_{11}}{2}\tilde{\epsilon}_3^{\mathrm{s}}(q, z_m) + \frac{C_{12}}{2}\tilde{\epsilon}_1^{\mathrm{s}}(q, z_m)\right\}\tilde{u}_3^{\mathrm{s}}(q, z_m) \tag{21}$$

with

$$\tilde{\epsilon}_1^{\mathrm{s}}(q, z) = -q\tilde{u}_1^{\mathrm{c}}(q, z), \tag{22}$$

$$\tilde{\epsilon}_3^{\mathrm{s}}(q, z) = \partial_3\tilde{u}_3^{\mathrm{s}}(q, z), \tag{23}$$

$$\tilde{\epsilon}_5^{\mathrm{c}}(q, z) = \partial_3\tilde{u}_1^{\mathrm{c}}(q, z) + q\tilde{u}_3^{\mathrm{s}}(q, z). \tag{24}$$

Thus, for the surface layer

$$\tilde{\epsilon}_1^{\mathrm{s}}(q, z_m) = -q\tilde{u}_1^{\mathrm{c}}(q, z_m), \tag{25}$$

$$\begin{aligned}\tilde{\epsilon}_3^{\mathrm{s}}(q, z_m) = {} & r\,\frac{\cosh^2(qz_m) - r(qz_m)^2 - 1}{||f(z_m)||}\, q\tilde{u}_1^{\mathrm{c}}(q, z_m)\\ & + (1 - r)\,\frac{\cosh(qz_m)\sinh(qz_m) + rqz_m}{||f(z_m)||}\, q\tilde{u}_3^{\mathrm{s}}(q, z_m),\end{aligned} \tag{26}$$

$$\tilde{\varepsilon}_5^{\mathrm{c}}(q,\, z_{\mathrm{m}}) = (1\,+\,r)\,\frac{\cosh(qz_{\mathrm{m}})\sinh(qz_{\mathrm{m}})\,-\,rqz_{\mathrm{m}}}{||f\,(z_{\mathrm{m}})||}\,q\tilde{u}_1^{\mathrm{c}}(q,\, z_{\mathrm{m}}) + \frac{(1\,-\,r)\sinh^2(qz_{\mathrm{m}})\,-\,2(rqz_{\mathrm{m}})^2}{||f\,(z_{\mathrm{m}})||}\,q\tilde{u}_3^{\mathrm{s}}(q,\, z_{\mathrm{m}}), \tag{27}$$

where

$$r \equiv \frac{1\,-\,s}{1\,+\,s} \tag{28}$$

and

$$||f\,(qz)|| \equiv f_1\,(qz)f_3\,(qz)\,+\,f_2^2\,(qz) = \cosh^2(qz)\,-\,(rqz)^2\,-\,1. \tag{29}$$

Gathering all expressions entering the elastic energy leads to

$$v_{\mathrm{el}} = \frac{q}{2}[\tilde{u}_1^{\mathrm{c}}(q,\, z_{\mathrm{m}}),\, \tilde{u}_3^{\mathrm{s}}(q,\, z_{\mathrm{m}})]\begin{bmatrix} M_{11}(qz_{\mathrm{m}}) & M_{13}(qz_{\mathrm{m}}) \\ M_{13}(qz_{\mathrm{m}}) & M_{33}(qz_{\mathrm{m}}) \end{bmatrix}\begin{bmatrix} \tilde{u}_1^{\mathrm{c}}(q,\, z_{\mathrm{m}}) \\ \tilde{u}_3^{\mathrm{s}}(q,\, z_{\mathrm{m}}) \end{bmatrix} \tag{30}$$

with

$$M_{11}(qz_{\mathrm{m}}) = (1\,-\,r)\,\frac{\cosh(qz_{\mathrm{m}})\sinh(qz_{\mathrm{m}})\,-\,rqz_{\mathrm{m}}}{||f\,(qz_{\mathrm{m}})||}C_{11}, \tag{31}$$

$$M_{13}(qz_{\mathrm{m}}) = \frac{1\,-\,r}{1\,+\,r}\,\frac{(1\,-\,r)\sinh^2(qz_{\mathrm{m}})\,-\,2(rqz_{\mathrm{m}})^2}{||f\,(qz_{\mathrm{m}})||}C_{11}, \tag{32}$$

$$M_{33}(qz_{\mathrm{m}}) = (1\,-\,r)\,\frac{\cosh(qz_{\mathrm{m}})\sinh(qz_{\mathrm{m}})\,+\,rqz_{\mathrm{m}}}{||f\,(qz_{\mathrm{m}})||}C_{11}, \tag{33}$$

which is a central result for GFMD simulations in which both normal and shear stresses are considered.

For reasons of completeness, we state the general elastic energy density

$$v_{\mathrm{el}} = \sum_{\mathbf{q}}\frac{q}{2}[\tilde{u}_1^{*}(\mathbf{q}),\, \tilde{u}_3^{*}(\mathbf{q})]\begin{bmatrix} M_{11}(qz_{\mathrm{m}}) & -\,\mathrm{i}M_{13}(qz_{\mathrm{m}}) \\ \mathrm{i}M_{13}(qz_{\mathrm{m}}) & M_{33}(qz_{\mathrm{m}}) \end{bmatrix}\begin{bmatrix} \tilde{u}_1(\mathbf{q}) \\ \tilde{u}_3(\mathbf{q}) \end{bmatrix}, \tag{34}$$

where $\tilde{u}(\mathbf{q})$ is now the complete, complex Fourier transform of the displacement of wavevector $\mathbf{q}$. For zero shear (normal) stress, the elastic energy is minimized with respect to the lateral (normal) displacement and thus becomes

$$v_{\mathrm{el}} = \frac{q}{2}\left\{M_{11}(qz_{\mathrm{m}}) - \frac{M_{13}^2(qz_{\mathrm{m}})}{M_{33}(qz_{\mathrm{m}})}\right\}|\tilde{u}_1(\mathbf{q})|^2 \quad \text{(zero normal stress)}, \tag{35}$$

$$v_{\mathrm{el}} = \frac{q}{2}\left\{M_{33}(qz_{\mathrm{m}}) - \frac{M_{13}^2(qz_{\mathrm{m}})}{M_{11}(qz_{\mathrm{m}})}\right\}|\tilde{u}_3(\mathbf{q})|^2 \quad \text{(frictionless contact)}. \tag{36}$$

2.3.1. Asymptotic analysis. It is instructive to consider various limits. First, for large wavevectors, the problem reduces to that of a semi-infinite solid. In this case, the quotients in equations (31)–(33) with $||f\,(qz_{\mathrm{m}})||$ in the denominator can be set to one and the elastic

energy is essentially q times an effective modulus times a squared displacement. More specifically, the $M_{ij}(qz_m)$ become

$$M_{11}(qz_m \gg 1) = \frac{2}{1+s} C_{44}, \tag{37}$$

$$M_{13}(qz_m \gg 1) = \frac{2s}{1+s} C_{44}, \tag{38}$$

$$M_{33}(qz_m \gg 1) = \frac{2}{1+s} C_{44}. \tag{39}$$

In the second limit, i.e. that of short wavevectors, we find

$$qM_{11}(z_m \ll 1) = \frac{C_{44}}{z_m}, \tag{40}$$

$$qM_{13}(z_m \ll 1) = 0, \tag{41}$$

$$qM_{33}(z_m \ll 1) = \frac{C_{11}}{z_m} \tag{42}$$

so that we may write for center-of-mass displacements

$$v_{el}(q=0) = \frac{C_{44}}{2z_m}\tilde{u}_1^2(0) + \frac{C_{11}}{2z_m}\tilde{u}_3^2(0). \tag{43}$$

This corresponds to the elastic energy—per unit area—of an isotropically deformed (and periodically repeated) solid being glued to a rigid substrate.

As a brief side aspect, let us also discuss the limiting case of $C_{44} = 0$ ($\Rightarrow r = 1$) which describes a compressible fluid. Given the prefactors in equations (31)–(33), one might have been tempted to set *all* $M_{ij}(qz_m)$ to zero. However, the just-presented asymptotic analysis reveals that this would not have lead to the correct result for $M_{33}(qz_m \to 0)$, which remains finite even for a vanishingly small shear modulus. Thus, the only mode necessitating elastic energy when altering the shape of the 'top layer' of a fluid is that which leads to a volume reduction, i.e., the $\tilde{u}_3(q=0)$ mode.

We conclude this section by making the link of our results to the contact modulus E^* introduced in equation (4). For semi-infinite solids, or large qz_m, the expression in the curly brackets in equation (36) reduces to $2(1-s)C_{44}$, which indeed can be shown to be half E^*. This implies that equation (36) is consistent with (4) in the limit of a frictionless semi-infinite contact.

3. Numerical results

3.1. Displacements in non-isotropic solids

To model a non-isotropic solid, we consider a cubic crystal with its (100) surface facing up. To make the comparison of continuum theory to full molecular dynamics (MDs) simulations as transparent as possible, we furthermore restrict ourselves to a simple cubic lattice in which each atom (which one may also see as a grid point) is connected to its nearest neighbors with a spring of stiffness k_1 and to next-nearest neighors with a spring of stiffness $k_2 = k_1$. Mechanical equilibrium of the springs is assumed at a distance a_0 between nearest neighbors and $\sqrt{2}\,a_0$ for next-nearest neighbors. With these definitions, it is readily seen that the elastic

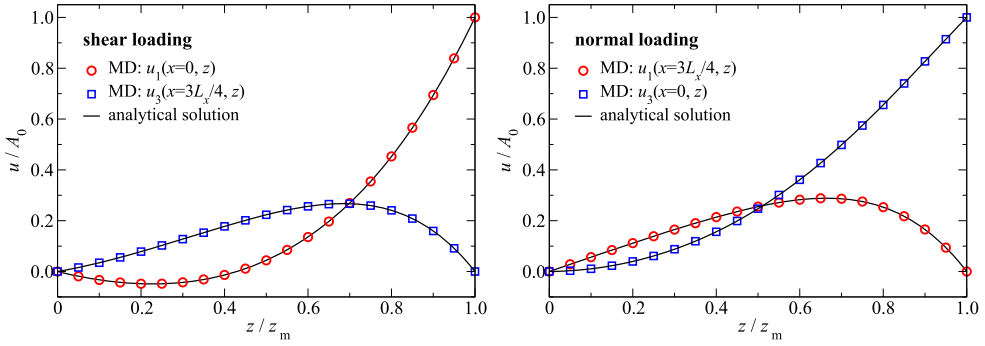

Figure 1. Lateral (red circles) and normal (blue squares) displacements $u_{1,3}$ at selected crosssections for shear (left) and normal (right) loading as obtained from MD simulations. The displacements are given in units of the maximum displacement A_0, which is valid at the top layer of the solids located at the normal coordinate $z = z_m = L_x/2$. The displacements are set to zero at the bottom layer ($z = 0$). Full lines represent the continuum solutions used to obtain internal stresses in GFMD simulations.

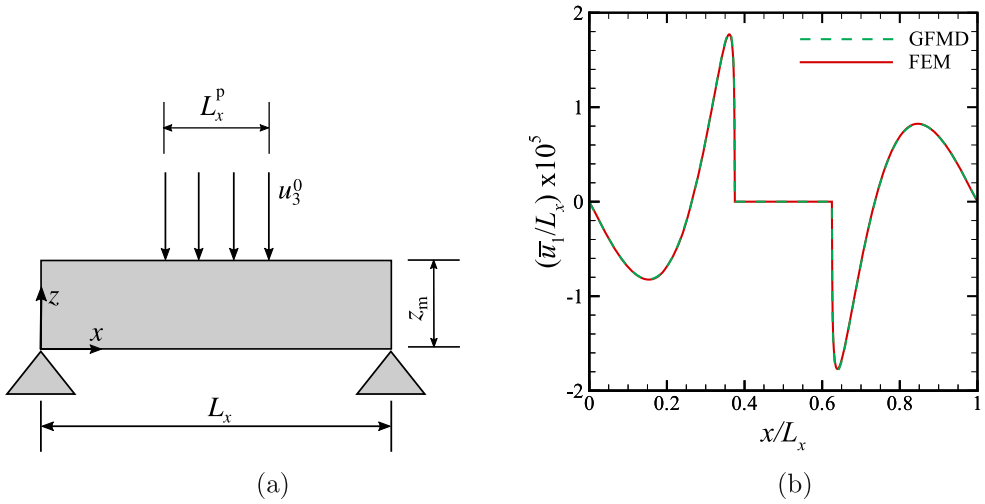

Figure 2. (a) Periodic unit cell of an isotropic slab indented by a flat rigid sticking punch. (b) The normalized tangential surface displacement $\bar{u}_1/L_x$ obtained using GFMD and FEM.

tensor—fully defined by $C_{11} = (k_1 + k_2)/a_0$ and $C_{12} = C_{44} = k_2/a_0$—violates the isotropy condition for the given choice of $k_1 = k_2$, since in this case $C_{44} > (C_{11} - C_{12})/2$. Here, the stiffness is divided by a_0 so that the elastic constants have the usual units.

In our example, we consider a slab of height $L_z = L_x/2$, where $L_x = 40a_0$ is the lateral length of the domain, which is repeated periodically along the x-direction. The just-defined system is solved with a self-written MD code, in which individual atoms are also coupled to damping linear in velocity. The mass of atoms is set to unity, the time step to 0.1 and damping to 0.25. Two cases of displacements in the top layer are treated: normal loading for which $u_1(x, z_m) = 0$, $u_3(x, z_m) = A_0 \cos(2\pi x/L_x)$ and shear loading for which

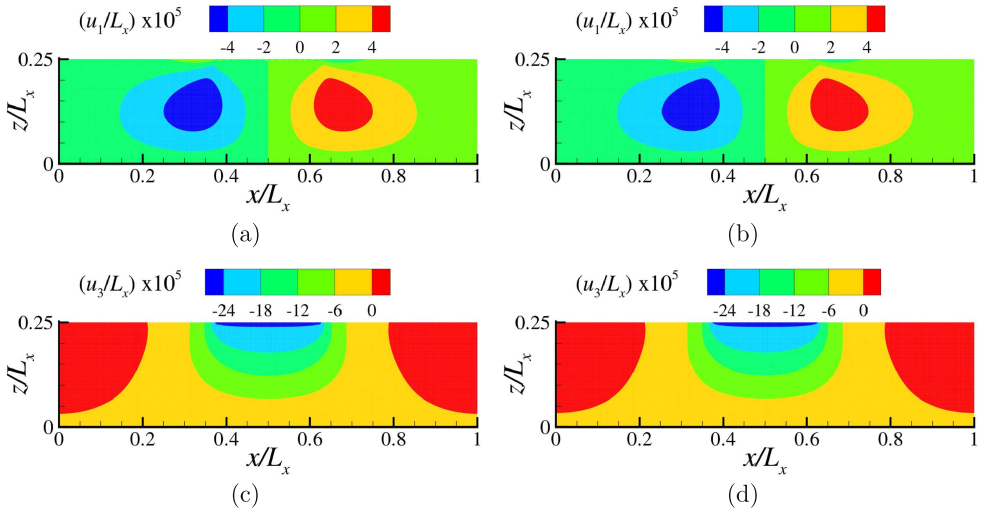

Figure 3. Displacement fields obtained using: (a), (c) GFMD and analytical solution; (b), (d) and FEM.

$u_1(x, z_m) = A_0 \cos(2\pi x/L_x)$, $u_3(x, z_m) = 0$. To justify the assumption of linear elasticity, the maximum displacement amplitude is set to $A_0 = a_0/100$. The bottom layer is kept fixed. The system relaxes after a few thousand time steps.

Agreement between full MD and the analytical expressions for the displacement fields is clearly revealed in figure 1.

3.2. Displacement and stress fields in isotropic solids

As a benchmark problem to compare GFMD to FEM we here consider the indentation of an isotropic elastic two-dimensional slab by an array of flat rigid punches. Contact between punches and slab is taken to be fully sticking. The analysis is performed on a periodic unit cell with fixed bottom as shown schematically in figure 2(a).

Normal displacement is prescribed at the contact of length L_x^p:

$$u_3(x, z_m) = u_3^0 \qquad \text{for} \qquad \frac{L_x - L_x^p}{2} < x < \frac{L_x + L_x^p}{2}. \tag{44}$$

The slab is indented to $u_3^0/L_x = 2.5 \times 10^{-4}$. Outside the contact region, the top surface is traction free. The aspect ratio of the slab, which is taken to have the elastic properties of aluminum, $C_{11} = 105$ GPa and $s = C_{44}/C_{11} = 0.25$, is $a = z_m/L_x = 1/4$, and the rigid punch is $L_x^p/L_x = 1/4$. For the finite-element analysis the slab is discretized using a uniform mesh of square elements. The number of degrees of freedom is $n_{dof} = 2nnx \times nnz$, where nnx is the number of nodes in x-direction, and nnz the number of nodes in z-direction. For the GFMD simulation the surface is discretized using nx equispaced grid points, with $nx = nnx$. Contact between the rigid indenters and the slab is modeled through a hard-wall potential. The static solution is found in GFMD using damped dynamics as described in [11]. The damping factor η used in this simulations is

$$\eta_x = \eta_z = \eta_0 \frac{1}{\tau\sqrt{nx}}, \tag{45}$$

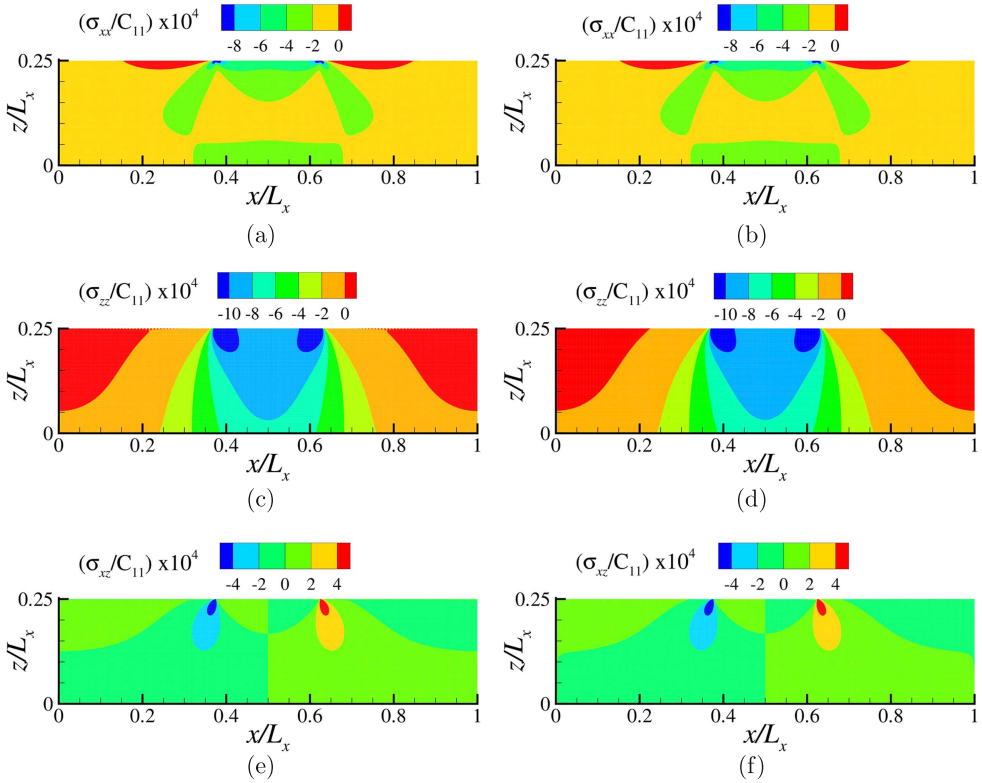

Figure 4. Stress fields obtained using: (a), (c), (e) GFMD and analytical solution; (b), (d), (f) and FEM.

where η_0 is the damping prefactor and τ is the time step. The damping prefactor is selected such that the slowest mode is slightly under-damped in z-direction. The number of MD iterations used to reach convergence scales as $n_{\mathrm{it}} \sim O(\sqrt{nx})$ and the time step is $\tau = 0.25$. The normalized lateral surface displacement $\bar{u}_1/L_x$ obtained by the two methods is shown for $nnx = nx = 1024$ in figure 2(b). The over bar indicates the value of the variable at the surface. No differences can be seen by the naked eye.

The displacement and stress fields inside the body for the GFMD simulations are calculated using equations (12)–(16) and (25)–(27). For a better comparison with FEM, the fields are evaluated at all locations inside the body corresponding to the nodes in the FEM calculation. The body fields hence obtained are compared with those obtained using FEM in figures 3 and 4.

3.3. Convergence rate and simulation time

The convergence rate is studied considering the calculation of the L_2 norm of the surface displacement,

$$\|\bar{u}_1\|_{L_2} = \sqrt{\sum_{i=1}^{nx} u_1(x_i,\, z_{\mathrm{m}})^2}\,. \tag{46}$$

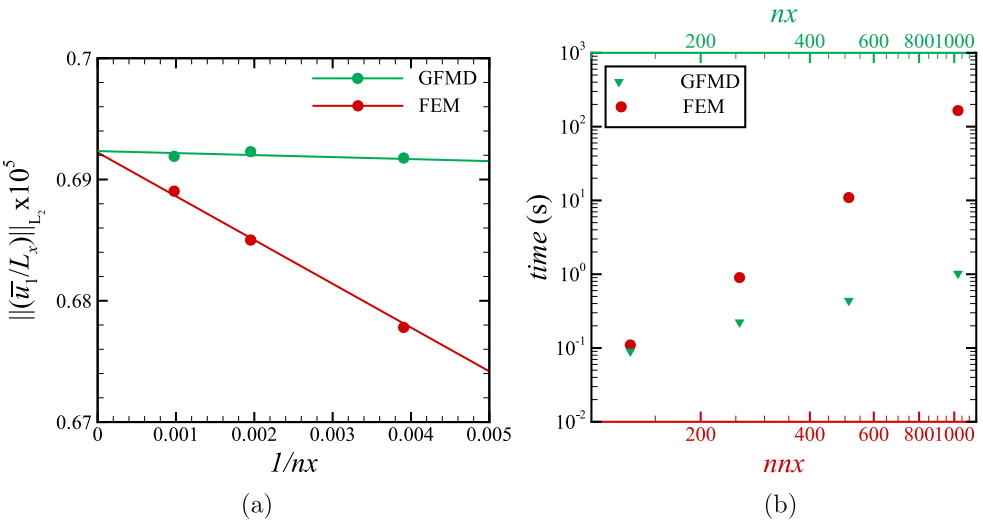

Figure 5. (a) The L_2 norm of tangential surface displacement obtained using GFMD and FEM are plotted as a function of $1/nx$ (b) Simulation time for GFMD compared with FEM.

Following [19], the error in the norm obtained using FEM as a function of the degrees of freedom in the simulation can be written as:

$$\|(\bar{u}_1/L_x)\|_{L_2}^{\text{FEM}} - \|(\bar{u}_1/L_x)\|_{L_2}^{\text{exact}} \approx \frac{\kappa}{n_{\text{dof}}^{\beta}}. \tag{47}$$

The exact solution, the asymptotic rate of convergence β, and the prefactor κ, are obtained by linearly fitting three data points corresponding to $nnx = 256, 512, 1024$. As expected [19], given that the mesh refinement is uniform and the order of the interpolating polynomial for the shape functions is one, the asymptotic rate of convergence is found to be 0.5:

$$\|(\bar{u}_1/L_x)\|_{L_2} = \left(0.692 - \frac{2.552}{n_{\text{dof}}^{0.5}}\right) \times 10^{-5}. \tag{48}$$

Since the finite-element mesh has square elements, it follows that

$$\frac{1}{nnx} = \left(\frac{2a}{n_{\text{dof}}}\right)^{0.5}. \tag{49}$$

We can therefore rewrite the L_2 norm as

$$\|(\bar{u}_1/L_x)\|_{L_2} = \left(0.692 - \frac{2.552}{(2a)^{0.5}}\frac{1}{nnx}\right) \times 10^{-5}, \tag{50}$$

which allows for direct comparison with GFMD (see figure 5(a)). The order of convergence with respect to the discretization of the two methods is found to be the same, while the prefactors are favorable for GFMD, i.e. $\kappa/L_x = -3.609 \times 10^{-5}$ for FEM while $\kappa/L_x = -1.653 \times 10^{-5}$ for GFMD. Figure 5(b) shows the simulation time as a function of the surface discretization. The results are all obtained on a single Intel Xeon(R) 3.10 GHz processor with 31.3 Gbytes of RAM. The GFMD simulations are found to be faster than FEM, and the computational advantage increases with increasing system size. In addition to

this, a smaller number of grid points are needed in GFMD to obtain the same results as in FEM. For the simulation reported here, if we decide to tolerate an error $e = 0.005$ in the L_2 norm of lateral surface displacement, the GFMD simulations require $nx = 128$ grid points while the FEM simulations need $nnx = 1024$ surface nodes. This results in a GFMD simulation being 1650 times faster than FEM.

It is to be noted here that: (1) we have not searched for the optimal meshing scheme to solve the finite-element problem, simply used a mesh with squared elements for ease of comparison with the equi-spaced surface grid points used in GFMD; (2) the speed of the finite-element simulation depends heavily on the solver used. Here we have used a direct sparse solver with skyline storage, where the time consuming step is the factorization of the skymatrix. The order of factorization in a skyline solver is generally $O((nnx\ B)^2)$ [20] where B is the mean bandwidth, which cannot exceed nnx. We are aware that for large systems, an iterative solver would be much more cost-effective. In GFMD, the computational complexity scales with $O(nx\sqrt{nx}\log nx)$, (3) the speed of the GFMD simulation depends on the choice of the damping factors, which in general are different in the x and z-direction. The optimal damping factor to obtain critical damping of the system depends on the loading, the height of the slab and the elastic constants. We here simply considered a single damping factor that would critically damp the modes in z-direction, and thus under-damp the modes in x-direction.

4. Conclusions

GFMD, a fastly converging boundary value method used to compute contact pressures and surface displacements of incompressible continuum semi-infinite solids, is here extended to apply to finite solids with generic Poisson's ratio and boundary conditions. Moreover, the body fields can now be computed analytically from the tractions and/or surface displacements. This extension allows the GFMD technique to provide the same information that can be obtained through the FEM, but with a significant gain in simulation time.

An additional advantage of GFMD is that for typical contact problems, where the contact area evolves during the simulation, the contact can be easily captured and simply described by means of an interaction potential. We have here used a hard-wall potential, but one can also model the bodies in contact explicitly and apply an interaction potential, as the Xu–Needleman [21], where the contact response in normal direction is coupled to that in tangential direction.

An interesting application that can be envisaged for the GFMD method, in virtue of the extensions presented in this paper, is the replacement of the FEM in discrete dislocation plasticity simulations of contact. This has the potential to significantly increase the time efficiency of the discrete dislocation plasticity calculations by that allowing to extend the applicability of such models to bodies of larger size, and with a realistic surface profile.

Acknowledgments

This project has received funding from the European Research Council (ERC) under the European Union's Horizon 2020 research and innovation programme (grant agreement no. 681813).

References

[1] Karpov E G, Wagner G J and Liu W K 2004 *Int. J. Numer. Methods Eng.* **62** 1250–62
[2] Campañá C and Müser M H 2006 *Phys. Rev.* B **74** 075420
[3] Kong L T, Bartels G, Campañá C, Denniston C and Müser M H 2009 *Comput. Phys. Commun.* **180** 1004–10
[4] Park H S, Karpov E G and Liu W K 2005 *Int. J. Numer. Methods Eng.* **64** 237–59
[5] Pastewka L, Sharp T A and Robbins M O 2012 *Phys. Rev.* B **86** 075459
[6] Karpov E G, Park H S and Liu W K 2007 *Int. J. Numer. Methods Eng.* **70** 351–78
[7] Benassi A, Vanossi A, Santoro G E and Tosatti E 2010 *Phys. Rev.* B **82** 081401
[8] Kajita S, Washizu H and Ohmori T 2012 *Phys. Rev.* B **86** 075453
[9] Campañá C and Müser M H 2007 *Europhys. Lett.* **77** 38005
[10] Pastewka L, Prodanov N, Lorenz B, Müser M H, Robbins M O and Persson B N J 2013 *Phys. Rev.* E **87** 062809
[11] Prodanov N, Dapp W B and Müser M H 2014 *Tribol. Lett.* **53** 433–48
[12] van der Giessen E and Needleman A 1995 *Modelling Simul. Mater. Sci. Eng.* **3** 689
[13] Akarapu S, Sharp T and Robbins M O 2011 *Phys. Rev. Lett.* **106** 204301
[14] Carbone G and Mangialardi L 2008 *J. Mech. Phys. Sol.* **56** 684–706
[15] Carbone G, Lorenz B, Persson B N J and Wohlers A 2009 *Eur. Phys. J.* E **29** 275–84
[16] Putignano C, Carbone G and Dini D 2015 *Int. J. Solids Struct.* **69–70** 507–17
[17] Persson B N J 2001 *J. Chem. Phys.* **115** 3840–61
[18] Born M and Huang K 1998 *Dynamical Theory of Crystal Lattices* (*International Series of Monographs on Physics*) (Oxford: Clarendon) https://books.google.nl/books?id=5q9iRttaaDAC
[19] Szabo B and Babuška I 1991 *Finite Element Analysis* (New York: Wiley-Interscience, Wiley) https://books.google.nl/books?id=JsCg-QWUT28C
[20] Synn S Y and Fulton R E 1995 *Comput. Syst. Eng.* **6** 275–84
[21] Xu X P and Needleman A 1993 *Modelling Simul. Mater. Sci. Eng.* **1** 111